

All-Optical Tunability of Metalenses Permeated with Liquid Crystals

Giovanna Palermo,[#] Andrew Lininger,[#] Alexa Guglielmelli, Loredana Ricciardi, Giuseppe Nicoletta, Antonio De Luca, Joon-Suh Park, Soon Wei Daniel Lim, Maryna L. Meretska, Federico Capasso,* and Giuseppe Strangi*



Cite This: <https://doi.org/10.1021/acsnano.2c05887>



Read Online

ACCESS |

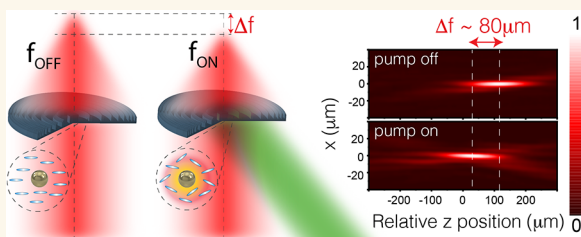
Metrics & More

Article Recommendations

Supporting Information

ABSTRACT: Metasurfaces have been extensively engineered to produce a wide range of optical phenomena, allowing exceptional control over the propagation of light. However, they are generally designed as single-purpose devices without a modifiable postfabrication optical response, which can be a limitation to real-world applications. In this work, we report a nanostructured planar-fused silica metalens permeated with a nematic liquid crystal (NLC) and gold nanoparticle solution. The physical properties of embedded NLCs can be manipulated with the application of external stimuli, enabling reconfigurable optical metasurfaces. We report the all-optical, dynamic control of the metalens optical response resulting from thermoplasmonic-induced changes of the NLC solution associated with the nematic–isotropic phase transition. A continuous and reversible tuning of the metalens focal length is experimentally demonstrated, with a variation of $80 \mu\text{m}$ (0.16% of the 5 cm nominal focal length) along the optical axis. This is achieved without direct mechanical or electrical manipulation of the device. The reconfigurable properties are compared with corroborating numerical simulations of the focal length shift and exhibit close correspondence.

KEYWORDS: metalens, metasurface, reconfigurable, thermoplasmonics, liquid crystal, tunable



INTRODUCTION

Traditionally, the propagation of light is controlled by refractive optical elements.¹ Recently, a paradigm shift has been realized through the introduction of optical metasurfaces, enabling the development of flat optical components by controlling the propagation of light at the nanoscale.^{2–10}

Once a given frequency of interest has been set, the desired optical response can be engineered by manipulating the geometry and position of subwavelength structures (meta-elements) on the surface. Each meta-element of the metasurface acts as an individual resonator or truncated waveguide, resulting in local control over the transmitted phase and amplitude at high spatial resolution.¹¹ These advances have led to the fabrication of ultrathin metalenses with focusing properties matching or exceeding those of typical refractive lenses.^{12–14} Metasurfaces have been implemented in a range of passive (nontunable/nondynamic) applications, such as focusing and imaging,^{15,16} beam conversion,¹⁷ and holography.¹⁸ However, these devices are typically created to support a fixed electromagnetic response which is determined at the time of fabrication. This limitation can be overcome by designing reconfigurable systems, or metasurface devices supporting a dynamically modifiable optical response. Post-

fabrication tunability can unlock a range of potential applications, including varifocal imaging, beam steering, dynamic aberration correction, and dynamic holography.^{19,20} The dynamic response is typically controlled by an external stimulus; common control methods for creating reconfigurable systems involve thermal, electrical, chemical, or mechanical action.^{21–24}

Nematic liquid crystals (NLCs) are well-known materials in which the refractive index can be modified through the application of an external stimulus, such as an electric or magnetic field.²⁵ In a typical NLC cell, the liquid crystal is infiltrated between two glass slides that have been properly functionalized in order to obtain the desired molecular alignment.²⁶ NLCs are known to exhibit a tunable refractive index due to reorientation of the molecular alignment. This tunable refractive index can be utilized to achieve active

Received: June 15, 2022

Accepted: October 6, 2022



ACS Publications

© XXXX American Chemical Society

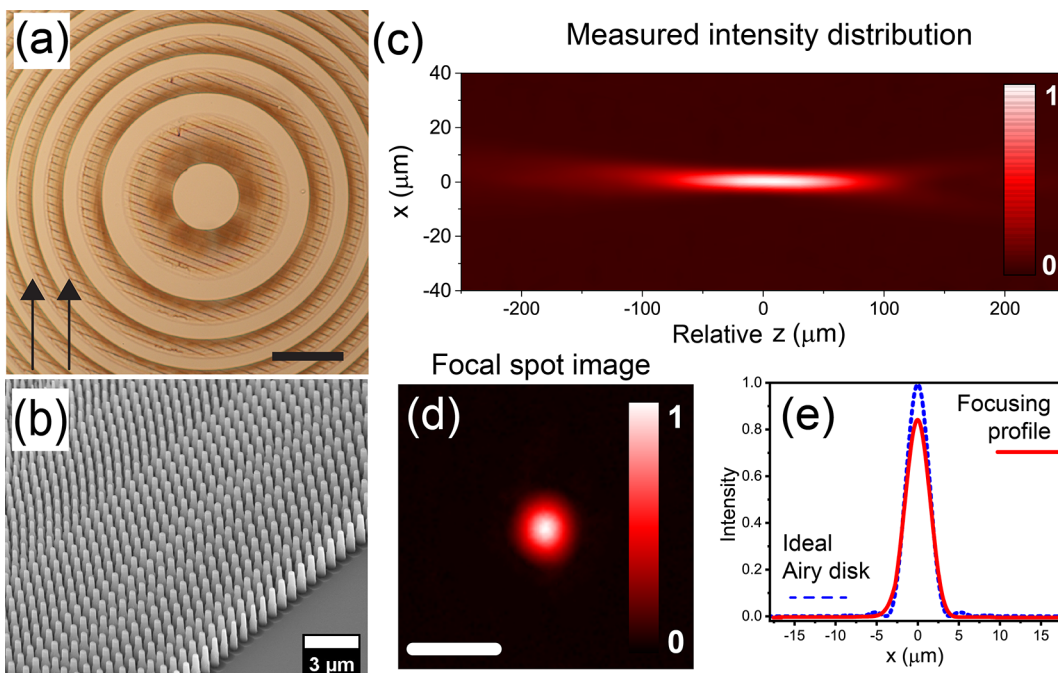


Figure 1. (a) Polarized optical microscopy image (with metalens between parallel polarizers (0°), shown as parallel arrows) of the central region of the empty metasurface; scale bar: $200\ \mu\text{m}$. (b) Scanning electron microscopy image of the pillar structure along the metasurface outer edge. (c) Experimentally measured intensity distribution in the x - z plane about the focal point (linear intensity scale). (d) Experimentally measured focal spot produced by the empty metasurface in the focal plane (scale bar: $10\ \mu\text{m}$) and (e) measured point spread function for the empty metasurface; dashed lines represent the focal spot profile for ideal Airy disk. The Strehl ratio is 0.835.

reconfigurable control over optical metasurface devices. One recent technique to integrate NLCs and metasurfaces is to replace one of the two glass plates in a conventional NLC cell with a metasurface device. The far-field optical properties of the metasurface, including diffractive lensing, can then be modified by electrically driving the NLC orientation state, similar to the operating principle of a liquid crystal (LC) display.^{27–29} Additionally, NLC-encapsulated metasurface devices have been programmed as individually addressable pixels. With this technology, electrical modification of adjacent cells, resulting in a manipulation of the local phase, has been used to dynamically create arbitrary holographic patterns.³⁰ Proceeding beyond these approaches, which utilize a thick NLC bulk, in this work we present a metasurface device which achieves dynamic and reversible reconfiguration by infiltrating NLC molecules into the space between the nanopillars composing the metasurface. In this scheme, the metasurface creates an initial phase profile for light focusing and the infiltrated NLC provides tunability. Having a thick LC superstrate, as in previously published devices, potentially introduces a large transmitted phase accumulation in the bulk LC material equal to that of many wavelengths, increasing the device performance sensitivity to nonuniformities in the thick LC layer. Thick LC layers also introduce significant scattering effects, negating some of the advantages of metasurface devices including aberration free focusing. By removing the bulk NLC cell, the metasurface retains its 2D configuration and the phase and amplitude control occurs solely within the metasurface as opposed to the superstrate.³¹ This allows for a more precise degree of control over the wavefront of light, without undue bulk phase accumulation.

Spherical gold nanoparticles (AuNPs) are ideal candidates for approaches requiring spatially confined heating and thermally triggered processes.^{32–35} The AuNP diameter can

be selected to tune the plasmonic band into the visible region, maximizing the absorption cross-section and resultant photo-thermal heating.³⁶ Plasmonic photothermal (PPT) heating is a direct consequence of localized surface plasmon resonance (LSPR), a distinct property of metallic nanoparticles. LSPR is an electromagnetic resonance generated by light interacting with conductive nanoparticles smaller than the incident wavelength.^{37,38} When these nanoparticles are embedded in thermoresponsive materials, they can be used to trigger thermally induced phenomena.³⁹

In particular, AuNPs can be used to induce thermoplasmonic effects in NLCs since the behavior of thermotropic NLCs is dependent on temperature: a phase transition can be induced by heating (from nematic to isotropic phase) or by cooling (from isotropic to nematic phase). During the nematic–isotropic (N–I) phase transition, the liquid crystal is converted from an ordered spatial distribution where the molecules align their long axis parallel to the substrate (planar or homogeneous alignment) to a disordered (isotropic) configuration without an alignment.²⁵ It should be noted that the pillar structure of the metasurface can disrupt the planar alignment since the LC molecules will interact with the interface at the pillar surface, leading to local deviations from the global alignment. This first-order phase transition modifies the physical properties of the liquid crystal, including the refractive index, density, and wetting properties.⁴⁰ For metasurface devices embedded with NLC, the phase transition can be harnessed to enable dynamic reconfigurability, greatly expanding the application space for these devices.

Here, we present a photothermally controlled varifocal metasurface infiltrated with a mixture of 4-hexyl-4'-biphenylcarbonitrile (6CB) NLC and AuNPs, that focuses light in the visible. Dynamic tunability of the focal distance is achieved through photothermal control of the NLC phase using free-

space illumination, exploiting the photoinduced phase transition due to the excitation of an LSPR mode on the AuNPs. This all-optical method offers a suitable alternative for various applications requiring compact and tunable focusing devices, avoiding mechanical actuators or dedicated electrical connections.²⁹ The system performance has been characterized in terms of the quality of the focus and focal length tunability range, and the reversibility and repeatability of the effect are demonstrated. The experimental results are further compared with corroborating numerical simulations of the infiltrated metasurface system focusing properties.

RESULTS AND DISCUSSION

The metasurface considered here is an all-glass metasurface with 1 cm diameter and a 5 cm focal length ($NA = 0.1$), designed to operate in air. The metasurface has been previously fabricated and characterized.¹⁴ The structure is composed of an array of fused-silica nanopillars with diameters ranging from 250 to 600 nm and a height of 2 μm , arranged in concentric rings, with a fixed pillar edge-to-edge distance of 250 nm. A morphological characterization of the “empty” metasurface (air among the nanopillars) is reported in Figure 1a,b. An optical microscopy image of the central region of the metasurface (Figure 1a) acquired between parallel polarizers (indicated with parallel arrows), which enhances the visual contrast as a function of pillar density, shows the concentric rings of densely spaced pillars interspersed with empty concentric rings, which were incorporated in the original design methodology. The structure and arrangement of the silica nanopillars within a central ring is shown via scanning electron microscopy (Figure 1b). A schematic of the optical setup used to characterize the focal spot and the intensity distribution of the metasurface is reported in the Supporting Information (Figure S1). The full spatial intensity distribution has been measured within $\pm 250 \mu\text{m}$ from the experimental focal length (Figure 1c). The focusing properties of the metasurface are further characterized by the experimental point-spread function (PSF) at the focal plane (Figure 1d). The focusing profile, characterized by a Strehl ratio (SR) of 0.835 ± 0.002 is shown in Figure 1e, exhibiting diffraction-limited performance. The Strehl ratio was calculated using curve fitting to the experimental PSF.

The metasurface was first infiltrated (Figure 2) with a mixture of 4-hexyl-4'-biphenylcarbonitrile (6CB) NLC and AuNPs (<1 wt %). 6CB is characterized by a crystalline-nematic transition temperature of $T_{\text{CrN}} = 13.64^\circ\text{C}$ and a N-I transition temperature of $T_{\text{NI}} = 28.07^\circ\text{C}$.^{41,42} At room temperature ($T \sim 20^\circ\text{C}$), the birefringence of 6CB is ~ 0.16 , with ordinary and extraordinary refractive indices of 1.53 and 1.70, respectively.⁴³ The temperature-dependent refractive indices of 6CB at $\lambda = 589 \text{ nm}$ are reported in the Supporting Information (Figure S2). A colloidal solution of spherical AuNPs (diameter $\sim 34 \text{ nm}$) dispersed in ethanol was synthesized, placing the LSPR mode in the green region of the visible spectrum (see Supporting Information). The optical absorption (Figure S3) and photothermal conversion have been investigated. This series of photothermal measurements (see Supporting Information Figure S4) revealed a strong linear correlation between laser intensity and photoinduced temperature increase of AuNPs along with optimal thermal stability.

The infiltration of the metasurface with pure LC was previously reported by Lininger et al.⁴⁴ For the current experiment, several droplets of the NLC/AuNPs mixture in the isotropic phase (heated to $T > 30^\circ\text{C}$) were placed round the outer edge

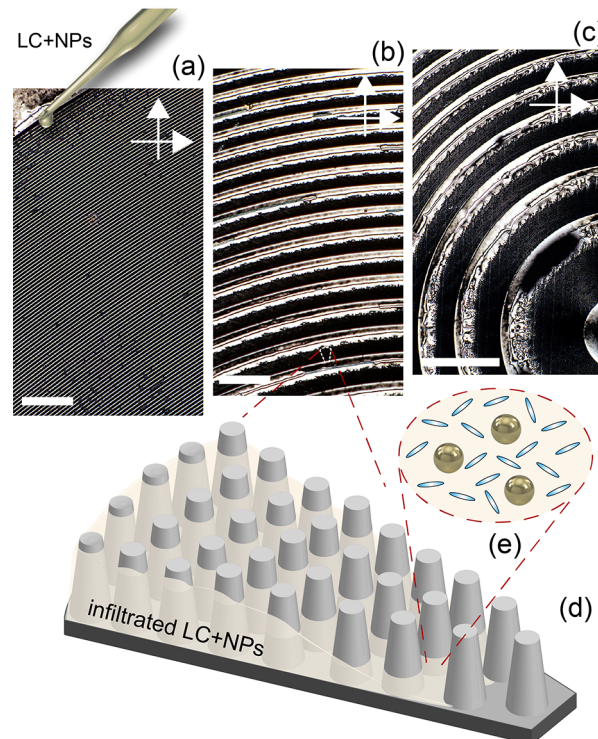


Figure 2. Polarized optical microscopy (with the metasurface between crossed polarizers (90°), shown as perpendicular arrows) image of 6CB+AuNPs filled metasurface along the (a) far edge, (b) inner, and (c) central region; scale bar: 200 μm . The pipet in (a) illustrates a droplet of LC placed at the edge of the lens during the infiltration procedure. (d) Illustration of a pillars region of the metasurface infiltrated with the 6CB+AuNPs mixture (e).

of the metasurface and left to infiltrate on a hot plate for 1 h. During the infiltration, the NLC tends to move radially inward from the point of introduction at the outer edge of the lens after fully infiltrating the external pillared rings and remains spatially nonuniform even after the NLC front reaches the center of the lens. The equilibrium height profile of the infiltrated NLC strongly depends on the radially varying width of the circumferential rings without nanopillars (channels), due to the wicking forces and the downward force from the droplet at the outer edge of the lens.^{45,46} The infiltration of the mixture inside the metasurface can be followed through an optical microscope analysis of the metasurface between crossed polarizers. After the 6CB+AuNPs infiltration, the metasurface is visibly brighter under cross-polarization due to the polarization conversion performed by the birefringent NLC (Figure 2). It is possible to recognize different optical textures along the edge (Figure 2a), inner (Figure 2b), and central region (Figure 2c) of the system. In the regions without the nanopillars, a schlieren texture is observed, characterized by a series of point and line disclinations and appearing as dark brushes against a bright background. This texture is common for parallel LC alignment in unrubbed cells.⁴⁷ It is distinct from the more uniform and darker texture observed in the regions with nanopillars.

The optical setup to control the infiltrated NLC includes a continuous wave green pump laser, on resonance with the AuNP LSPR. The light impinges at an angle of 45° to the sample and the resulting temperature variations are monitored via a thermal camera (see Figure 3a). The green pump laser is

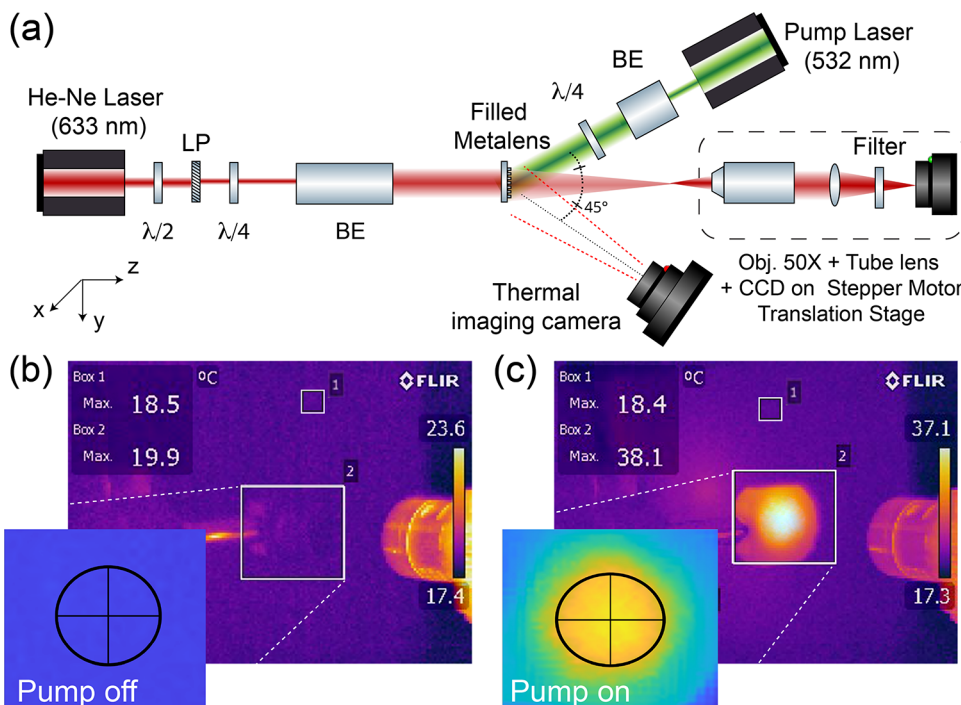


Figure 3. (a) Schematic diagram of the all-optical pump probe and thermographic setup: linear polarizer (LP), $\lambda/2$ and $\lambda/4$ waveplates, and beam expander (BE); thermographic images of the 6CB+AuNPs filled metalens (b) when the pump laser beam is stopped (pump off) and (c) when the pump laser beam impinges on the sample (pump on, steady-state) with intensity $I = 2.3 \text{ W/cm}^2$. Inset: Temperature maps of the metalens sample (black circle) in each pump configuration, linear scale.

enlarged with a beam expander (BE) to illuminate the entire surface of the metalens (beam diameter = 1 cm). A circular polarization state was used for the pump beam (including a $\lambda/4$ waveplate). This setup ensures consistent absorption for all planar NLC configurations and minimizes any strain on the NLC orientation.⁴⁸ This is necessary since a planar configuration was observed for the infiltrated NLC (molecules aligned in the x - y plane).²⁵ A 570 nm high-pass filter is placed before the imaging CCD to remove the scattered pump beam from the focusing profile.

Figure 3b shows a thermographic image of the 6CB+AuNPs filled metalens (with the mounting device) when the pump beam is stopped (pump off). The two white square regions of interest, indicated as (1) and (2) in the figure, represent the two measurement regions centered on the ambient room temperature (18.5 ± 1.0 °C) and on the sample (19.9 ± 1.0 °C), respectively. The sample is then illuminated with the pump beam (pump on) and the intensity is varied and monitored until a maximum steady-state photoinduced temperature of 38.1 ± 1.0 °C is reached on the sample (Box 2 in Figure 3c). The target temperature, obtained at a pump beam intensity of 2.3 W/cm^2 , is greater than the NI transition temperature of $T_{\text{NI}} = 28.07$ °C, ensuring the thermotropic transition of the NLC to the isotropic phase.

A characterization of the focusing profile along the beam path of the 6CB+AuNPs infiltrated metalens is reported in Figure 4. Figure 4a shows the 3D reconstruction of the experimental intensity distribution from the metalens in the absence of the pump beam (pump off 1), with the focal plane at the z -position (along the optical axis) of 110 μm (Figure 4d). The z -position is given relative to the experimental zero point. The corresponding beam profile shows a full-width half-maximum (fwhm) of $4.2 \pm 0.2 \mu\text{m}$ (Figure 4g). The 3D beam

reconstruction is obtained by acquiring images in the x - z plane in the range $-250 \mu\text{m} < \text{relative } z < +250 \mu\text{m}$ along the optical axis, with a fixed step movement of 2 μm . Comparing the infiltrated metalens (Figure 4d) with the empty metalens prior to infiltration (Figure 1c), the infiltration is seen to decrease the quality of the focusing profile (decreasing Strehl ratio). However, the focal profile does not appear significantly altered further by the photothermal control procedure. The observed low Strehl ratio focusing behavior is expected since the metalens has not been specifically designed to accommodate the infiltrated NLC. Thus, the infiltration disrupts the designed phase profile, and likewise the focusing performance. The quality of the focus can be further quantified by comparing the modulation transfer function for the several PSFs (presented in the Supporting Information).

When turning on the pump beam, a shift of 80 μm is observed in the focal distance (new z -position= 30 μm), as well as a modification of the PSF (Figure 4b). Modifications in the sidelobe intensity can be observed in the focal plane 2D intensity distribution (Figure 4e), while the fwhm of the central spot is decreased with respect to the pump off case. The fwhm of the focal spot is evaluated to be $3.8 \pm 0.2 \mu\text{m}$ (see Figure 4h). The pump beam is then removed from the sample in order to probe the reversibility of the tuning effect. A 3D reconstruction of the intensity distribution and the corresponding PSF and the intensity sectional profile in the x -direction at the focal plane are reported in Figure 4c,f,i, respectively. Following the heating cycle (pump off 2) the focal plane returns to the z -position of 110 μm (Figure 4c), as obtained before the heating cycle (Figure 4a). The fwhm of the obtained PSF focal spot is $4.5 \pm 0.2 \mu\text{m}$ (Figure 4i). The corresponding Strehl ratio values, for the three reported measurements, are SR = 0.324 ± 0.002 for pump off 1, SR =

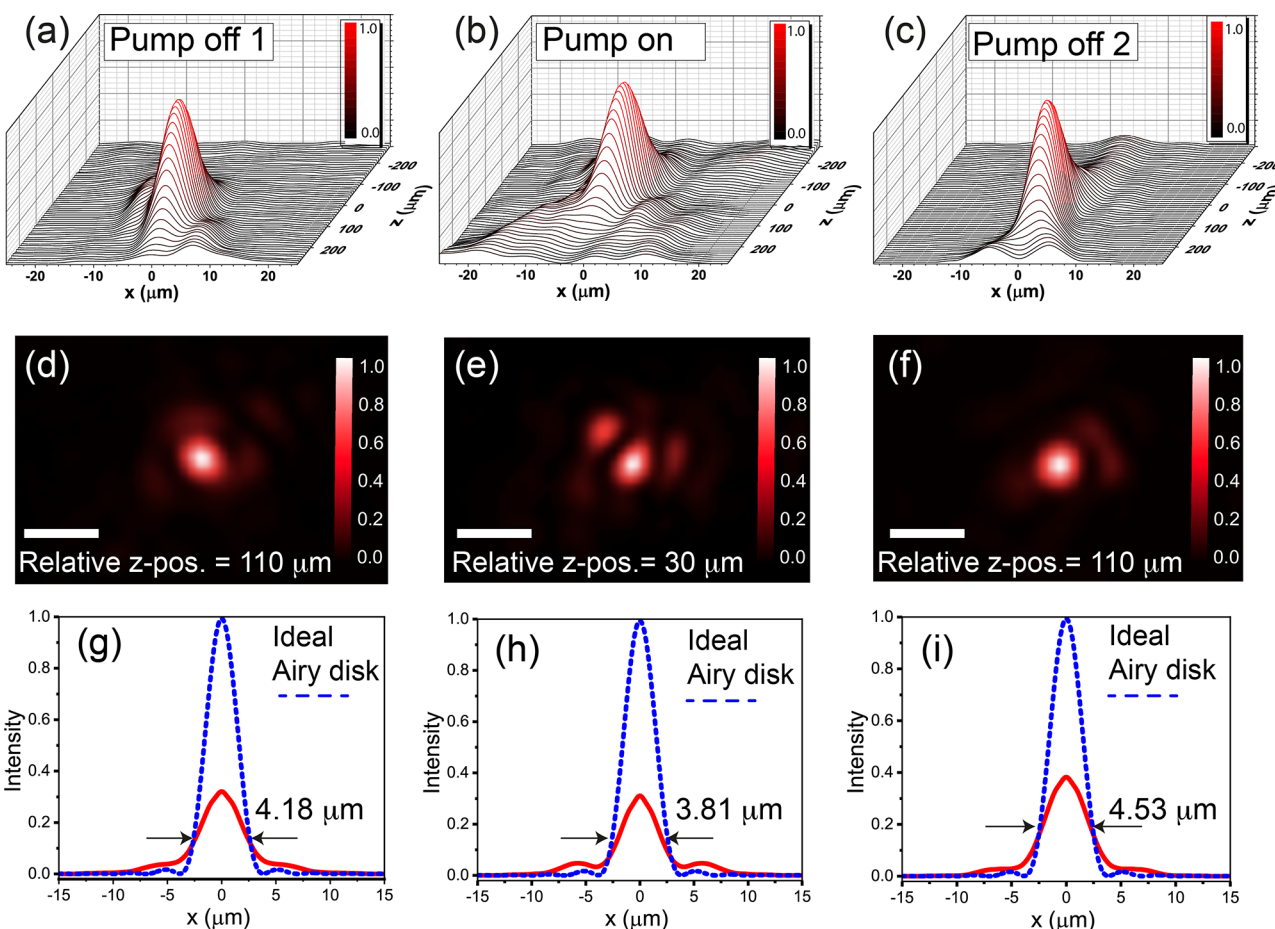


Figure 4. 3D plot of the measured intensity distributions of the 6CB+AuNPs filled metalens (a) before, (b) during, and (c) after the exposure to the pump laser beam with (d–f) the corresponding intensity distributions at the focal plane (z -position is relative to the experimental zero point) for the three cases (scale bar: 10 μm) and (g–i) the corresponding PSFs, respectively. The blue dashed lines represent the focal spot profile for ideal Airy disk along with the experimental focusing profile in red (ideal fwhm = 3.23 μm). Experimental Strehl ratio values: (g) 0.324, (h) 0.315, and (i) 0.386.

0.315 ± 0.002 for pump on, and SR = 0.386 ± 0.002 for pump off 2. The focal length tunability for the 6CB+AuNPs infiltrated metalens system is similarly demonstrated in Figure 5a.

In order to further investigate the repeatability and reversibility of the tuning effect, a dynamic thermo-optical experiment was performed by monitoring the intensity in a fixed x - y plane (z -position = 30 μm) while modifying the sample temperature. The temperature was altered by controlling the exposure time to the pump beam. In the time interval of 0–60 s, a temperature of 40 $^{\circ}\text{C}$ is reached, which is sufficient to induce the N–I transition (Figure 5b, top panel). The intensity value is obtained by integrating over the intensity distribution in the x - y plane, and the measurement is then iterated for two on/off cycles. Only one cycle is shown in Figure 5b, bottom panel, for clarity. Increasing the temperature of the sample from $T_1 = 20$ $^{\circ}\text{C}$ to $T_7 = 40$ $^{\circ}\text{C}$, the focal spot intensity is seen to increase roughly 7-fold from the initial intensity (Figure 5b, bottom panel). Once the pump beam is removed the NLC cools back to room temperature, returning to the nematic phase (blue side region of the graph). At the same time, the light intensity values are observed to return to the initial state, demonstrating the repeatability of the observed effect. A control experiment (same experimental conditions) was performed on an NLC-filled metalens without AuNPs, and

no significant temperature or intensity variations were observed. This result demonstrates that the photoheat conversion is directly associated with the plasmonic photothermal effect of the AuNPs.

The proposed tunable metalens system can be exploited for varifocal imaging with photothermally controlled focusing. To validate the imaging ability of the tunable metalens system a negative 1951 USAF resolution target (R3L3S1N, Thorlabs) was imaged with the metalens in place of an imaging objective (the imaging setup schematic is reported in Figure S5). The images (corresponding to group 4 of the resolution target) formed by the metalens are shown in Figure 6. Initially, when the pump laser is off, the image is in maximal focus at z -position = 110 μm (Figure 6a). When the thermo-optical control is switched on, the image moves out of focus (Figure 6b). The image is returned to focus once the pump laser is removed (Figure 6c). Similarly, with the acquisition plane at the z -position of 30 μm , the obtained image is out of focus when the pump beam is off (Figure 6d) and in focus when the pump beam is on (Figure 6e). The image is again removed from focus when the pump beam is turned back off (pump off 2) (Figure 6f). The observed distance between the two well-focused image planes confirms a shift of about 80 μm in the focal length induced by the photothermal effects.

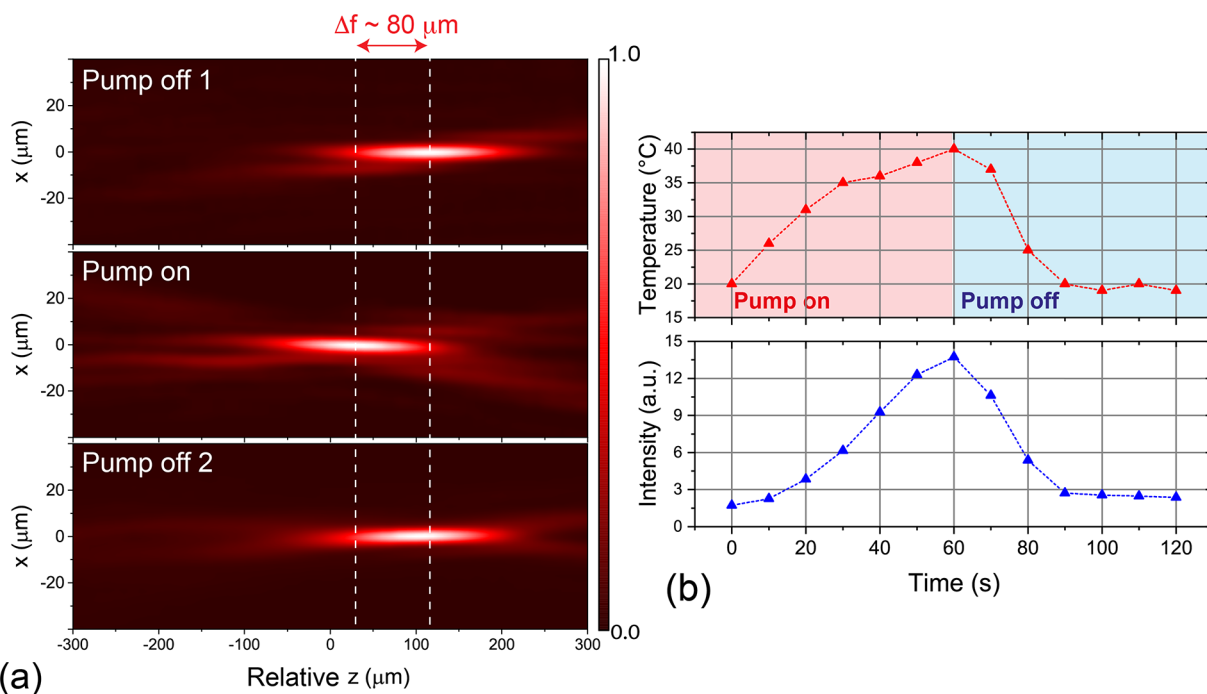


Figure 5. (a) Normalized measured intensity distributions along the propagation direction in the x - z plane for the 6CB+AuNPs filled metalens before (pump off 1), during (pump on), and after (pump off 2) the sample is exposed to the pump beam ($\lambda = 532 \text{ nm}$). The z -position is relative to the experimental zero point. (b) Variations in the temperature and integrated focal spot intensity at the focal plane of the pump-active metalens (z -position = $30 \mu\text{m}$), as the pump beam is turned on (pump on) and then back off (pump off) at 60 s .

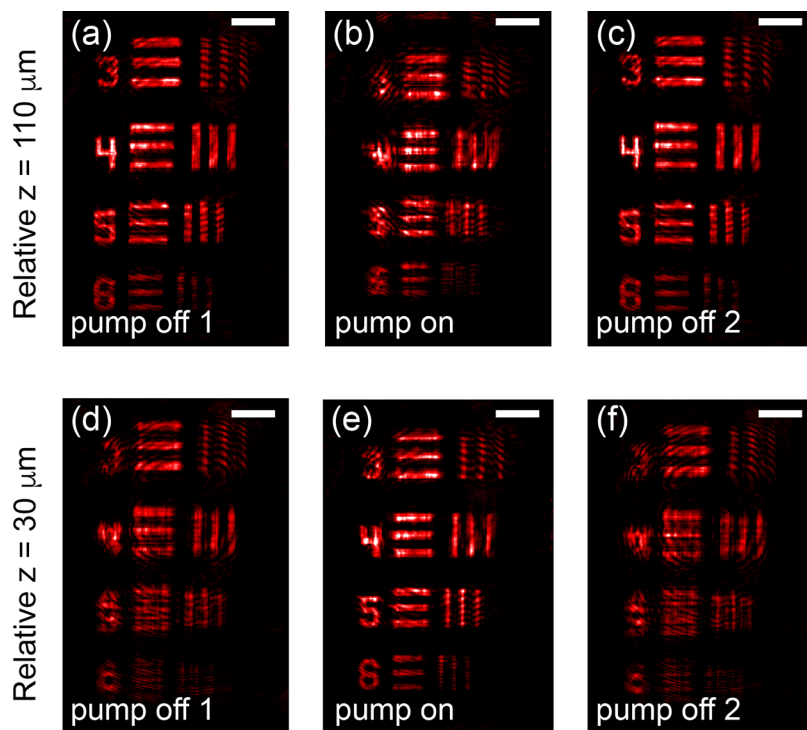


Figure 6. Experiments showing the tuning of the imaging distance of the metalens. The target image (USAF 1951 target, group 4), at relative z -position = $110 \mu\text{m}$ is (a) in focus when the pump beam is off (pump off 1), (b) out of focus when the pump beam is on, and (c) again in focus when the pump beam is turned back off (pump off 2). In a similar manner, the target image at relative z -position = $30 \mu\text{m}$ is (d) out of focus when the pump beam is off, (e) in focus when the pump beam is on, and (f) again out of focus when pump beam is turned back off. The scale bar is $400 \mu\text{m}$. Note that some speckle is present due to the coherent illumination.

Optical Simulations. Simulations of the metalens optical properties have been conducted using a finite-difference time-domain method (MEEP).⁴⁹ Each distinct combination of pillar

radius, in-plane spacing, infiltration height, and liquid crystal refractive index was simulated independently, and the amplitude and phase of the transmitted light were computed

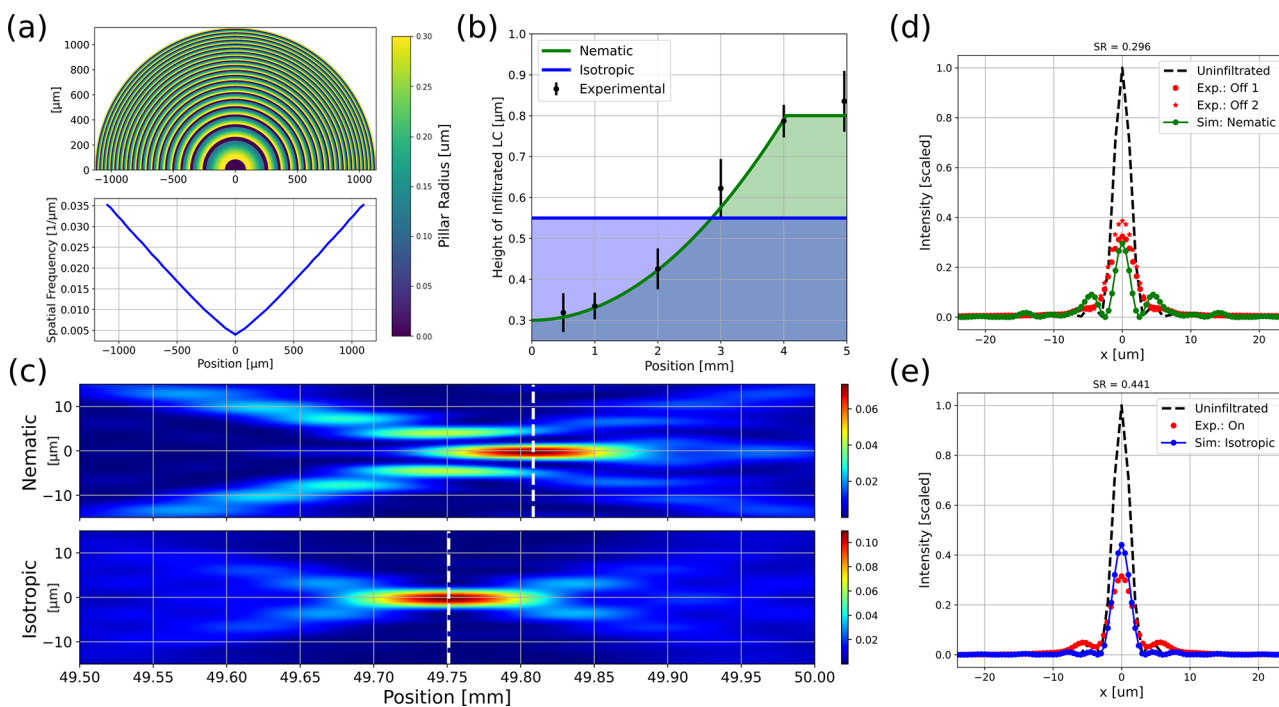


Figure 7. Optical simulations of the infiltrated metasensor, including the reconfigurability associated with the N–I transition. (a) Illustration of the metasensor structure. (Top) Color map of the radius of the fabricated pillars for the central ~ 1 mm radial section of the metasensor. Note the concentric bands of pillars and nonpillared regions. The colorbar represents the nanopillar radii in μm . (Bottom) Spatial frequency of the pillar bands increases with radial distance from the center. This corresponds to decreasing the widths of the nonpillared rings, affecting the infiltration. (b) Filling profiles considered in the simulations are shown for the entire metasensor radius. In the nematic phase, we assume the LC to follow a quadratically increasing radial infiltration profile, reaching a maximum height of $0.8 \mu\text{m}$ at 4 mm from the center. We also assume the isotropic phase LC is at a constant infiltration height ($0.55 \mu\text{m}$) with the same volume as the nematic phase LC. The theoretical infiltration profile is compared with experimental phase compensator measurements of the infiltrated LC in the nematic phase. (c) Comparison of the far-field spatial intensity distributions calculated for each of the infiltration profiles above. Focusing behavior is illustrated for both the nematic (top) and isotropic (bottom) simulations. The peak intensity (arb. units) is similar for both focal spots, as is the depth of focus. A clear shift of $\sim 60 \mu\text{m}$ is demonstrated between the two simulations. (d,e) Comparison of the PSF for both nematic (d) and isotropic (e) simulations. Each case is compared with the PSF obtained from a similar simulation of the uninfiltrated metasensor. A clear decrease in peak intensity with respect to the uninfiltrated focusing abilities is observed. This is reflected in the calculated Strehl ratios of 0.296 and 0.441, respectively. The theoretical PSFs are qualitatively similar to the experimental results.

at a distance of 2λ above the metasurface. It is seen that NLC material infiltrated into the structure greatly affects the phase transmission properties, introducing an additional phase profile superimposed upon the designed metasensor hyperbolic phase profile. The individual pillar responses were configured with the known metasensor geometry to obtain the total transmitted near-field, and vectorial diffraction propagation was applied to calculate the far-field intensity distribution near the focal point. The metasensor was simulated in free space (no infiltration) and with 6CB infiltration at both the ordinary ($n = 1.53$) and isotropic ($n = 1.58$) refractive indices. More details on the simulation procedure can be found in the [Supporting Information](#) (simulation procedures).

The infiltration profile is dependent upon the hemiwicking (wetting) properties of the metasurface. This process describes the spreading of liquid on a patterned surface as driven by spontaneous capillary action.^{50,51} The rate and degree of spreading depends on both the interfacial interaction energy for the liquid-glass and liquid-air interfaces, as well as the viscoelasticity of the NLC.⁴⁵ In addition, the structured nanoscale geometry of the surface critically influences the hemiwicking process.⁴⁶ In these simulations, we have assumed that the NLC follows an increasing radial infiltration profile, as illustrated in Figure 7a,b. The profile increases quadratically from the center of the metasensor, leveling off at 80% (4 mm) of

the total radial distance. This choice of filling profile is consistent with the geometry of the metasensor, considering the radially increasing spatial frequency of the pillar bands combined with the hemiwicking properties (Figure 7a) and experimental phase compensator measurements of the liquid crystal infiltration height (details in the [Supporting Information](#)).⁴⁴ We acknowledge that this choice of filling profile is not distinct, and experimental deviations from the profile are probable. However, the quadratic profile serves as a useful low-order model to parametrize the device geometry. The maximum height of the infiltrated nematic phase of 6CB is assumed to be 40% of the total pillar height ($0.80 \mu\text{m}$), corresponding to a relatively low volumetric degree of infiltration.

The properties of the NLC are known to change when undergoing the first order nematic–isotropic (N–I) phase transition, as predicted by Landau–de Gennes theory.^{52–54} Here, we assume that the effect of the N–I transition is to alter the refractive index ($n = 1.58$) and decrease the NLC viscoelasticity and surface tension at the liquid-glass interface. This can lead to a “smoothing” of the radial infiltration profile in the isotropic phase, which we approximate as a constant height of infiltration at the same total volume (28%, $0.55 \mu\text{m}$). This modification of the infiltration profile affects the additional phase profile introduced by the infiltrated NLC.

Again, we acknowledge that a completely smooth infiltration is not necessarily realistic to the experimental case since the infiltrated profile depends on the specific experimental details of the infiltration. Any deviations from the constant profile will likely increase aberrations in the far-field. However, we propose that the combination of coexisting phase profiles from the fabricated lens and the infiltrated NLC is one possible explanation for the observed reconfigurable focusing behavior. This point is further discussed in the *Supporting Information* (Mechanism of Coexisting Phase Profiles).

The far-field intensity profiles and PSFs corresponding to these systems are shown in *Figure 7c–e*. Considering the N–I transition, we observe a shift in the focal point of $\sim 60\ \mu\text{m}$ along the optical axis when passing from the nematic to isotropic phase. This focal point shift is similar to the experimental result (0.12% compared to 0.16% of the nominal focal length, respectively, and in the same axial direction). Interestingly, the depth of focus and maximal intensity of the main focal spot remain largely unchanged throughout the transition. Nonideal focusing behavior in the form of aberrations near the focal spot are noted in both cases. Similar intensity aberrations are observed in the experimental data, although the specific location and intensity of these effects are highly dependent on the specifics of the infiltrated profile and unlikely to be captured by simulation. The resulting PSFs are shown in *Figure 7d,e*, along with the experimental profiles. A clear focusing behavior is observed; however, the infiltration of LC into the metasurface structure is seen to affect the quality of the focus. The theoretical focusing efficiencies (defined as the power passing through 3 Airy disk diameters at the focal plane, relative to the incident power) are calculated as 18 and 20%. In both cases, the infiltration leads to an increase in the sidelobe intensity. This is reflected in the Strehl ratios of 0.30 and 0.44 for the nematic and isotropic profiles, respectively. These values are similar to the experimental Strehl ratios of 0.36 and 0.32 (± 0.06 and 0.12, respectively). The modulation transfer functions for the calculated PSFs are shown in the *Supporting Information*. The consistently low Strehl ratios in both theory and experiment are reflective of nonideal focusing behavior in the metasurface system. This is expected behavior and occurs because the metasurface utilized in this work has not been specifically designed to integrate the phase induced by the NLC infiltration, causing the infiltrated NLC to disrupt the designed phase profile.⁴⁴

CONCLUSIONS

We report a nanostructured metasurface device permeated with a nematic liquid crystal and gold nanoparticle solution. A dynamic, reversible, and all-optical control of the lens focal length is demonstrated via a light-induced thermoplasmonic effect. A total focal shift of $80\ \mu\text{m}$ in the focal length is observed. This work is a significant step toward all-optical tunable metasurfaces by expanding the working range from the near-infrared to the visible regime. In comparison to existing systems, this device offers an all-optical tunable metasurface in which the NLC+AuNPs mixture is directly infiltrated into the metasurface structure without the necessity of assembling a bulky LC cell. This leaves the 2D flat surface of the metasurface unchanged, without a bulk LC superstrate. Furthermore, this metasurface system is fully compatible with conventional CMOS fabrication techniques and is simple to control in comparison to tunable devices based on mechanical stretching or other control methods.

The metasurface device has been experimentally demonstrated for imaging. Future applications include adaptive vision, bioimaging, and display applications where varifocal or multiplane imaging is desired. The imaging results could be improved by tuning the fabricated silica structure to better accommodate the optical properties of the infiltrated LC, increasing the quality of the focus under various illumination conditions. In the current system, the phase profile is offset from the designed target by the infiltrated LC material. In an ideal system the pillar structure would be designed such that the target phase profile is achieved after the LC is infiltrated with a typical height profile. To improve the focal point shift distance, pillar geometries can be designed which maximize the difference in transmitted phase due to the LC phase transition. Altering the pillar arrangement will also alter the hemiwickling properties of the nanostructure, which could be designed for specific infiltration profiles. Optimization methods, in particular, multi-objective machine learning approaches, would be useful for this task.

Finally, the experimental results are compared with corroborating numerical simulations of the infiltrated metasurface device focusing properties. These simulations offer an explanation of the reconfigurable focusing properties of the device; however, some assumptions of the model (particularly the specific infiltration profile) are not distinctive and do not necessarily reproduce the experimental case.

METHODS

Liquid Crystal and Nanoparticle Preparation. Citrate-stabilized AuNPs with an average diameter of $34 \pm 2\ \text{nm}$ were synthesized following the well-developed kinetically controlled seeded growth method,⁵⁵ via the reduction of HAuCl_4 by sodium citrate. All chemicals were purchased from Sigma-Aldrich. The synthesized AuNPs were purified by ultrafiltration (Vivaspin20 equipped with a 100 kDa membrane) and then dispersed in spectrofluorimetric grade ethanol with a final concentration of 2 nM. The AuNP solution was added to 4-hexyl-4'-biphenylcarbonitrile (6CB) NLC at 1 wt % and the solvent was evaporated to produce the NLC + AuNP mixture. More details on the AuNP and NLC preparation can be found in the *Supporting Information*.

Experimental Heating and Focusing Measurement. Heating of the infiltrated lens was performed with a continuous wave green laser ($\lambda = 532\ \text{nm}$, Verdi, Coherent) with circular polarization, at $I = 2.3\ \text{W/cm}^2$. The light impinges upon the sample at a 45° angle of incidence. The temperature variations were monitored with a thermal imaging camera (E40 FLIR). The focusing was measured for 633 nm incident light (He-Ne, JDS Uniphase 1137P). A resposable microscope setup with a $50\times$ objective (Leica 566040, NA = 0.5) was utilized to measure the far-field intensity pattern.

Optical Simulations. Simulations of the metasurface's optical properties were conducted using MEEP, an open source finite-difference time-domain (FDTD) method package.⁴⁹ All combinations of the pillar radius, in-plane spacing, infiltration height, and liquid crystal refractive index were simulated independently. The amplitude and phase of the transmitted light were computed at a distance of 2λ above the metasurface. The far-field focusing pattern was simulated by combining the individual pillar light transmission for the known pillar geometry and infiltration profile and applying a far-field transformation. More details on the simulations can be found in the *Supporting Information*.

ASSOCIATED CONTENT

SI Supporting Information

The Supporting Information is available free of charge at <https://pubs.acs.org/doi/10.1021/acsnano.2c05887>.

Schematic diagram of the optical setup used to characterize the focal spot and the intensity distribution of the metalens; temperature-dependent refractive indices of 6CB at $\lambda = 589$ nm; synthesis and characterization of the AuNPs; photothermal characterization of the AuNPs; schematic diagram of the full experimental apparatus; experimental and theoretical MTF comparison; simulation procedures; mechanism of coexisting phase profiles; manipulating the focal point tunability by varying the infiltrate refractive index; experimental measurement of liquid crystal height; comparison with some other similar tunable metalens systems ([PDF](#))

AUTHOR INFORMATION

Corresponding Authors

Federico Capasso – Harvard John A. Paulson School of Engineering and Applied Sciences, Harvard University, Cambridge, Massachusetts 02138, United States;
Email: capasso@seas.harvard.edu

Giuseppe Strangi – Department of Physics, NLHT-Lab, University of Calabria and CNR-NANOTEC Istituto di Nanotecnologia, 87036 Rende, Italy; Department of Physics, Case Western Reserve University, Cleveland, Ohio 44106, United States; Email: giuseppe.strangi@case.edu

Authors

Giovanna Palermo – Department of Physics, NLHT-Lab, University of Calabria and CNR-NANOTEC Istituto di Nanotecnologia, 87036 Rende, Italy;  orcid.org/0000-0001-5649-735X

Andrew Lininger – Department of Physics, Case Western Reserve University, Cleveland, Ohio 44106, United States;  orcid.org/0000-0001-6401-7301

Alexa Guglielmelli – Department of Physics, NLHT-Lab, University of Calabria and CNR-NANOTEC Istituto di Nanotecnologia, 87036 Rende, Italy;  orcid.org/0000-0002-0792-659X

Loredana Ricciardi – CNR-NANOTEC Istituto di Nanotecnologia, 87036 Rende, Italy;  orcid.org/0000-0002-2724-9952

Giuseppe Nicoletta – Department of Physics, NLHT-Lab, University of Calabria and CNR-NANOTEC Istituto di Nanotecnologia, 87036 Rende, Italy

Antonio De Luca – Department of Physics, University of Calabria and CNR-NANOTEC Istituto di Nanotecnologia, 87036 Rende, Italy;  orcid.org/0000-0003-2428-9075

Joon-Suh Park – Harvard John A. Paulson School of Engineering and Applied Sciences, Harvard University, Cambridge, Massachusetts 02138, United States; Nanophotonics Research Centre, Korea Institute of Science and Technology, Seoul 02792, Republic of Korea;  orcid.org/0000-0002-3235-5450

Soon Wei Daniel Lim – Harvard John A. Paulson School of Engineering and Applied Sciences, Harvard University, Cambridge, Massachusetts 02138, United States;  orcid.org/0000-0003-1689-6860

Maryna L. Meretska – Harvard John A. Paulson School of Engineering and Applied Sciences, Harvard University, Cambridge, Massachusetts 02138, United States

Complete contact information is available at:
<https://pubs.acs.org/10.1021/acsnano.2c05887>

Author Contributions

#G.P. and A.L. contributed equally to this work

Notes

The authors declare no competing financial interest.

ACKNOWLEDGMENTS

We acknowledge support from the Ohio Third Frontier Project “Research Cluster on Surfaces in Advanced Materials” (RC-SAM) at Case Western Reserve University. A.L. and G.S. acknowledge financial support from the NSF Grant No. 1904592 “Instrument Development: Multiplex Sensory Interfaces Between Photonic Nanostructures and Thin Film Ionic Liquids”. G.P. acknowledges financial support from the “AIM: Attraction and International Mobility” PON R&I 2014-2020 Calabria. G.N. acknowledges financial support from the “Dottorati innovativi a caratterizzazione industriale” PON R&I FSE-FESR 2014-2020. A.G. acknowledges financial support from the “NLHT - Nanoscience Laboratory for Human Technologies” (POR Calabria FESR-FSE 14/20). S.W.D.L. is supported by A*STAR Singapore through the National Science Scholarship Scheme. The Harvard University authors were partially supported by the AFOSR MURI Grant No. FA9550-21-1-0312. This work was performed in part at the Cornell NanoScale Science & Technology Facility, a member of the National Nanotechnology Coordinated Infrastructure (NNCI), which is supported by the NSF (Grant No. NNCI-1542081). This work was performed in part at the Harvard University Center for Nanoscale Systems (CNS); a member of the National Nanotechnology Coordinated Infrastructure Network (NNCI), which is supported by the National Science Foundation under NSF award no. ECCS-2025158. This work made use of the High Performance Computing Resource in the Core Facility for Advanced Research Computing at Case Western Reserve University.

REFERENCES

- (1) Saha, S.; Shah, D.; Shalaev, V. M.; Boltasseva, A. Tunable Metasurfaces: Controlling Light in Space and Time. *Optics and Photonics News* **2021**, *32*, 34–41.
- (2) Yu, N.; Capasso, F. Optical metasurfaces and prospect of their applications including fiber optics. *Journal of Lightwave Technology* **2015**, *33*, 2344–2358.
- (3) Zhan, A.; Colburn, S.; Trivedi, R.; Fryett, T. K.; Dodson, C. M.; Majumdar, A. Low-contrast dielectric metasurface optics. *ACS Photonics* **2016**, *3*, 209–214.
- (4) Shalitout, A. M.; Kildishev, A. V.; Shalaev, V. M. Evolution of photonic metasurfaces: from static to dynamic. *JOSA B* **2016**, *33*, 501–510.
- (5) Kildishev, A. V.; Boltasseva, A.; Shalaev, V. M. Planar photonics with metasurfaces. *Science* **2013**, *339*, 1232009.
- (6) Lio, G. E.; Ferraro, A.; Ritacco, T.; Aceti, D. M.; De Luca, A.; Giocondo, M.; Caputo, R. Leveraging on ENZ Metamaterials to Achieve 2D and 3D Hyper-Resolution in Two-Photon Direct Laser Writing. *Adv. Mater.* **2021**, *33*, 2008644.
- (7) Lio, G. E.; Ferraro, A. LIDAR and Beam Steering Tailored by Neuromorphic Metasurfaces Dipped in a Tunable Surrounding Medium. *Photonics* **2021**, *8*, 65.
- (8) Yu, N.; Capasso, F. Flat optics with designer metasurfaces. *Nature materials* **2014**, *13*, 139–150.
- (9) Jeong, H.; Yang, Y.; Cho, H.; Badloe, T.; Kim, I.; Ma, R.-M.; Rho, J. Emerging advanced metasurfaces: Alternatives to conventional bulk optical devices. *Microelectron. Eng.* **2020**, *220*, 111146.
- (10) Genevet, P.; Capasso, F.; Aieta, F.; Khorasaninejad, M.; Devlin, R. Recent advances in planar optics: from plasmonic to dielectric metasurfaces. *Optica* **2017**, *4*, 139–152.

- (11) Chung, H.; Miller, O. D. Tunable metasurface inverse design for 80% switching efficiencies and 144 angular deflection. *ACS Photonics* **2020**, *7*, 2236–2243.
- (12) Khorasaninejad, M.; Aieta, F.; Kanhaiya, P.; Kats, M. A.; Genet, P.; Rousso, D.; Capasso, F. Achromatic metasurface lens at telecommunication wavelengths. *Nano Lett.* **2015**, *15*, 5358–5362.
- (13) Lin, D.; Fan, P.; Hasman, E.; Brongersma, M. L. Dielectric gradient metasurface optical elements. *science* **2014**, *345*, 298–302.
- (14) Park, J.-S.; Zhang, S.; She, A.; Chen, W. T.; Lin, P.; Yousef, K. M.; Cheng, J.-X.; Capasso, F. All-glass, large metalens at visible wavelength using deep-ultraviolet projection lithography. *Nano Lett.* **2019**, *19*, 8673–8682.
- (15) Wang, S.; Wu, P. C.; Su, V.-C.; Lai, Y.-C.; Chen, M.-K.; Kuo, H. Y.; Chen, B. H.; Chen, Y. H.; Huang, T.-T.; Wang, J.-H.; et al. A broadband achromatic metalens in the visible. *Nature Nanotechnol.* **2018**, *13*, 227–232.
- (16) Chen, W. T.; Zhu, A. Y.; Sanjeev, V.; Khorasaninejad, M.; Shi, Z.; Lee, E.; Capasso, F. A broadband achromatic metalens for focusing and imaging in the visible. *Nature Nanotechnol.* **2018**, *13*, 220–226.
- (17) Wu, P. C.; Zhu, W.; Shen, Z. X.; Chong, P. H. J.; Ser, W.; Tsai, D. P.; Liu, A.-Q. Broadband wide-angle multifunctional polarization converter via liquid-metal-based metasurface. *Advanced Optical Materials* **2017**, *5*, 1600938.
- (18) Ni, X.; Kildishev, A. V.; Shalaev, V. M. Metasurface holograms for visible light. *Nat. Commun.* **2013**, *4*, 2807.
- (19) He, Q.; Sun, S.; Zhou, L. Tunable/reconfigurable metasurfaces: physics and applications. *Research* **2019**, *2019*, 1849272.
- (20) Kim, J.; Seong, J.; Yang, Y.; Moon, S.-W.; Badloe, T.; Rho, J. Tunable metasurfaces towards versatile metalenses and metaholograms: a review. *Advanced Photonics* **2022**, *4*, 024001.
- (21) Kim, I.; Ansari, M. A.; Mehmood, M. Q.; Kim, W.-S.; Jang, J.; Zubair, M.; Kim, Y.-K.; Rho, J. Stimuli-responsive dynamic metaholographic displays with designer liquid crystal modulators. *Adv. Mater.* **2020**, *32*, 2004664.
- (22) Nemati, A.; Wang, Q.; Hong, M.; Teng, J.; et al. Tunable and reconfigurable metasurfaces and metadevices. *Opto-Electronic Advances* **2018**, *1*, 18000901.
- (23) Yu, P.; Li, J.; Zhang, S.; Jin, Z.; Schütz, G.; Qiu, C.-W.; Hirscher, M.; Liu, N. Dynamic Janus metasurfaces in the visible spectral region. *Nano Lett.* **2018**, *18*, 4584–4589.
- (24) Rensberg, J.; Zhang, S.; Zhou, Y.; McLeod, A. S.; Schwarz, C.; Goldflam, M.; Liu, M.; Kerbusch, J.; Nawrodt, R.; Ramanathan, S.; et al. Active optical metasurfaces based on defect-engineered phase-transition materials. *Nano Lett.* **2016**, *16*, 1050–1055.
- (25) De Gennes, P.-G.; Prost, J. *The Physics of Liquid Crystals*; Oxford University Press: New York, 1993.
- (26) Komar, A.; Fang, Z.; Bohn, J.; Sautter, J.; Decker, M.; Miroshnichenko, A.; Pertsch, T.; Brener, I.; Kivshar, Y. S.; Staude, I.; et al. Electrically tunable all-dielectric optical metasurfaces based on liquid crystals. *Appl. Phys. Lett.* **2017**, *110*, 071109.
- (27) Fan, C.-Y.; Chuang, T.-J.; Wu, K.-H.; Su, G.-D. J. Electrically modulated varifocal metalens combined with twisted nematic liquid crystals. *Opt. Express* **2020**, *28*, 10609–10617.
- (28) Shen, Z.; Zhou, S.; Li, X.; Ge, S.; Chen, P.; Hu, W.; Lu, Y. Liquid crystal integrated metalens with tunable chromatic aberration. *Advanced Photonics* **2020**, *2*, 036002.
- (29) Bosch, M.; Shcherbakov, M. R.; Won, K.; Lee, H.-S.; Kim, Y.; Shvets, G. Electrically actuated varifocal lens based on liquid-crystal-embedded dielectric metasurfaces. *Nano Lett.* **2021**, *21*, 3849–3856.
- (30) Li, J.; Yu, P.; Zhang, S.; Liu, N. Electrically-controlled digital metasurface device for light projection displays. *Nat. Commun.* **2020**, *11*, 3574.
- (31) Krasnok, A. Metalenses go atomically thick and tunable. *Nat. Photonics* **2020**, *14*, 409–410.
- (32) Baffou, G.; Quidant, R. Thermo-plasmonics: using metallic nanostructures as nano-sources of heat. *Laser & Photonics Reviews* **2013**, *7*, 171–187.
- (33) Baffou, G.; Cichos, F.; Quidant, R. Applications and challenges of thermoplasmonics. *Nat. Mater.* **2020**, *19*, 946–958.
- (34) Lio, G. E.; Palermo, G.; De Luca, A.; Caputo, R. Tensile control of the thermal flow in plasmonic heaters realized on flexible substrates. *J. Chem. Phys.* **2019**, *151*, 244707.
- (35) Palermo, G.; Pagnotto, D.; Ricciardi, L.; Pezzi, L.; La Deda, M.; De Luca, A. Thermoplasmonic effects in gain-assisted nanoparticle solutions. *J. Phys. Chem. C* **2017**, *121*, 24185–24191.
- (36) Baffou, G.; Quidant, R.; Girard, C. Heat generation in plasmonic nanostructures: Influence of morphology. *Appl. Phys. Lett.* **2009**, *94*, 153109.
- (37) Mayer, K. M.; Hafner, J. H. Localized surface plasmon resonance sensors. *Chem. Rev.* **2011**, *111*, 3828–3857.
- (38) Govorov, A. O.; Richardson, H. H. Generating heat with metal nanoparticles. *Nano today* **2007**, *2*, 30–38.
- (39) Palermo, G.; Guglielmelli, A.; Pezzi, L.; Cataldi, U.; De Sio, L.; Caputo, R.; De Luca, A.; Bürgi, T.; Tabiryan, N.; Umeton, C. A command layer for anisotropic plasmonic photo-thermal effects in liquid crystal. *Liq. Cryst.* **2018**, *45*, 2214–2220.
- (40) De Sio, L.; Cataldi, U.; Guglielmelli, A.; Bürgi, T.; Tabiryan, N.; Bunning, T. J. Dynamic optical properties of gold nanoparticles/cholesteric liquid crystal arrays. *MRS Commun.* **2018**, *8*, 550–555.
- (41) Oweimreen, G.; Morsy, M. DSC studies on p-(n-alkyl)-p'-cyanobiphenyl (RCB's) and p-(n-alkoxy)-p'-cyanobiphenyl (ROCB's) liquid crystals. *Thermochim. Acta* **2000**, *346*, 37–47.
- (42) Okumus, M.; Özgan, S. Investigation of the phase transition and absorption properties of liquid crystal hexylcyanobiphenyl/octylcyanobiphenyl mixtures. *Asian J. Chem.* **2013**, *25*, 3879.
- (43) Li, J.; Gauzia, S.; Wu, S.-T. High temperature-gradient refractive index liquid crystals. *Opt. Express* **2004**, *12*, 2002–2010.
- (44) Lininger, A.; Zhu, A. Y.; Park, J.-S.; Palermo, G.; Chatterjee, S.; Boyd, J.; Capasso, F.; Strangi, G. Optical properties of metasurfaces infiltrated with liquid crystals. *Proc. Natl. Acad. Sci. U. S. A.* **2020**, *117*, 20390–20396.
- (45) Kim, J.; Moon, M.-W.; Kim, H.-Y. Dynamics of hemiwicking. *J. Fluid Mech.* **2016**, *800*, 57–71.
- (46) Extrand, C.; Moon, S. I.; Hall, P.; Schmidt, D. Superwetting of structured surfaces. *Langmuir* **2007**, *23*, 8882–8890.
- (47) Nehring, J.; Saupe, A. On the schlieren texture in nematic and smectic liquid crystals. *Journal of the Chemical Society, Faraday Transactions 2: Molecular and Chemical Physics* **1972**, *68*, 1–15.
- (48) Durbin, S.; Arakelian, S.; Shen, Y. Optical-field-induced birefringence and Fredericksz transition in a nematic liquid crystal. *Phys. Rev. Lett.* **1981**, *47*, 1411.
- (49) Oskooi, A. F.; Roundy, D.; Ibanescu, M.; Bermel, P.; Joannopoulos, J. D.; Johnson, S. G. MEEP: A flexible free-software package for electromagnetic simulations by the FDTD method. *Comput. Phys. Commun.* **2010**, *181*, 687–702.
- (50) Kiss, E. Wetting and wicking. *Text. Res. J.* **1996**, *66*, 660–668.
- (51) Bico, J.; Thiele, U.; Quéré, D. Wetting of textured surfaces. *Colloids Surf., A* **2002**, *206*, 41–46.
- (52) Sen, A.; Sullivan, D. Landau–de Gennes theory of wetting and orientational transitions at a nematic–liquid–substrate interface. *Phys. Rev. A* **1987**, *35*, 1391.
- (53) Mukherjee, P.; Bose, T.; Ghose, D.; Saha, M. Inclusion of density variation in the Landau–de Gennes theory of the nematic–isotropic phase transition. *Phys. Rev. E* **1995**, *51*, 4570.
- (54) Ten Bosch, A.; Maissa, P.; Sixou, P. A Landau-de Gennes theory of nematic polymers. *J. Phys., Lett.* **1983**, *44*, 105–111.
- (55) Bastús, N. G.; Comenge, J.; Puntes, V. Kinetically controlled seeded growth synthesis of citrate-stabilized gold nanoparticles of up to 200 nm: size focusing versus Ostwald ripening. *Langmuir* **2011**, *27*, 11098–11105.